Journal of Earthquake Engineering

ISSN: (Print) (Online) Journal homepage: https://www.tandfonline.com/loi/ueqe20

Seismic Performance and Collapse Fragility of Balloon-Framed CLT School Building

Yuxin Pan, Md Shahnewaz & Thomas Tannert

JOURNAL OF EARTHQUAKE ENGINEERING
https://doi.org/10.1080/13632469.2022.2123067

Taylor & Francis
Taylor & Francis Group

Seismic Performance and Collapse Fragility of Balloon-Framed CLT School Building

Yuxin Pan [a], Md Shahnewaz [b], and Thomas Tannert [a]

[a]School of Engineering, University of Northern British Columbia, Prince George, British Columbia, Canada; [b]Fast + Epp, Vancouver, British Columbia, Canada

ABSTRACT

Most previous research on seismic performance of cross-laminated timber (CLT) structures focused on platform-type construction. This paper investigates the seismic performance and collapse risk of a balloon-framed CLT school building, designed for Vancouver, Canada. Incremental dynamic analysis was performed using a three-dimensional numerical model. Experimental data from connection- and wall-level tests were used to calibrate and validate the model. Twenty-one ground motions (crustal, subduction inslab, and interface) were selected. The results showed the building well met the 2% design drift limit. It had 4.2% probability of collapse at design level by considering uncertainties with a collapse margin ratio of 3.18.

ARTICLE HISTORY
Received 11 March 2022
Accepted 5 September 2022

KEYWORDS
Cross-laminated timber; nonlinear finite element model; subduction earthquake; incremental dynamic analysis; seismic risk

1. Introduction

1.1. Objective

As part of the British Columbia (BC) Ministry of Education's Seismic Mitigation Program, the Begbie Elementary School, located in Vancouver, BC, Canada, will be replaced with a new building that was designed and constructed using balloon-framed cross-laminated timber (CLT) shear walls as the primary lateral loading resisting system. This is one of few balloon-framed CLT structures in Canada; understanding the building's seismic performance, especially its collapse capacity under large earthquake risks, may inform further construction of similar typology.

The objective of this paper is to quantify the nonlinear seismic responses of the balloon-framed CLT building by performing non-linear time history analyses (NLTHA) and evaluate its damage potential at various intensity levels through Incremental Dynamic Analyses (IDA). Experimental data from connection-level and full-scale shear wall tests (Shahnewaz, Dickof, and Tannert 2021) were used to calibrate the numerical parameters and then used to validate the model. A suite of bidirectional input ground motion records that reflected the local seismic hazard of Vancouver, BC, were selected as analysis input.

1.2. Cross-Laminated Timber Construction

CLT panels are made of three or more layers of orthogonally glued dimensional lumbers (Brandner et al. 2016). CLT, originally developed in Austria in the 1990s, has been actively promoted in North America over the last decade to meet the demand for more sustainable construction. Compared to concrete and steel, CLT has a lower environmental footprint (Chen and Popovski 2020). Due to its high stiffness and strength, CLT can be used as shear walls in multistory buildings to resist lateral loads

CONTACT Yuxin Pan ceypan@ust.hk Department of Civil and Environmental Engineering, The Hong Kong University of Science and Technology, Clear Water Bay, Hong Kong, China

(e.g. earthquakes), also in high-seismic zones (Tannert et al. 2018). As CLT panels show rigid-body behaviour, the connections that provide ductility and energy dissipation govern the performance of CLT shear walls. Wall-to-floor connections are provided with hold-downs (HD) and wall base shear brackets (WB) using nails or self-tapping screws (STS), and wall-to-wall connections (SP) are commonly provided with nailed or screwed spline joints.

CLT structures can be erected using platform- or balloon-framed systems (Karacabeyli and Gagnon 2019). In platform assemblies, each floor is a platform for the story above with the walls attached to the floors. In balloon-framed construction, the walls are continuous over multiple stories with floors supported by ledgers. While platform-framed CLT construction is generally better understood and already incorporated into standards such as the Canadian Standard Engineering Design in Wood (CSA 2019); balloon framing is still less common.

Extensive research on platform-type CLT structures and its connections (e.g. Ceccotti et al. 2013; Flatscher, Bratulic, and Schickhofer 2015; Gavric, Fragiacomo, and Ceccotti 2015a; Jalilifar, Koliou, and Pang 2021; Latour and Rizzano 2015; Liu and Lam 2019; Mahdavifar et al. 2019; Pozza et al. 2018; Schneider et al. 2015; Shahnewaz et al. 2020; van de Lindt et al. 2019), together with a number of successful projects, demonstrated the effectiveness of the system to form a lateral load resisting system. As the gravity loads are cumulative, the total building height of the platform construction is limited by the compression perpendicular-to-grain resistance of the base floor. With the combination of stringent panel aspect ratios, more panels are needed, as a consequence, a large number of connections are required which leads to larger accumulating flexural deformation and makes on-site assembly more costly and time consuming (Karacabeyli and Gagnon 2019).

CLT balloon framing can offer solutions to these problems. Like reinforced concrete shear walls, the ductility and nonlinear deformation demand in balloon-type CLT buildings are concentrated at the bottom of the walls. The number of shear walls in a balloon-frame structure is lower, reducing the number of required connections. Additionally, the building height is no longer limited by the floor's compression perpendicular-to-grain strength (Karacabeyli and Gagnon 2019; Khajehpour, Pan, and Tannert 2021) and perpendicular-to-grain shrinkage, allowing the support of additional stories; therefore, balloon-framing is deemed an appropriate construction type for taller buildings.

However, research on the balloon-frame CLT buildings is still limited. Pei et al. (2019) conducted shake table tests on a two-story building with post-tensioned rocking walls and observed the intended damage at the maximum considered earthquake level. Li, Wang, and He (2022) conducted cyclic tests and developed analytical prediction models to predict the lateral load resistance of balloon-frame shear walls. Chen and Popovski (2020) proposed a mechanics-based analytical model based on static tests on walls with an aspect ratio up to 12:1. Shahnewaz, Dickof, and Tannert (2021) investigated the seismic behavior of two-story balloon frame CLT walls under monotonic and reversed cyclic loading; the walls exhibited nearly pure rocking behavior, which was not impeded by the ledgers attached at mid-height. Zhang, Pan, and Tannert (2021) developed numerical models for two high-rise balloon-type CLT buildings and showed that horizontal connections (i.e. wall-to-floor) had the largest impact on the building's dynamic behavior. To date, no research is available related to the seismic fragility and collapse risk assessment for balloon-type CLT building in high seismic regions.

1.3. Seismic Fragility Assessment

Seismic fragility is an effective tool to identify the vulnerability of structures subjected to earthquakes (Shahnewaz et al. 2020). A fragility function specifies the probabilistic relationship between structural collapse, or some limit state of interest with the level of earthquake as intensity measure (*IM*) (Baker 2015). The fragility curves are constructed by assuming a lognormal cumulative distribution function (CDF) (Ibarra and Krawinkler 2005):

$$P(C|\,IM\, =\, x)\, =\, \Phi\left(\frac{\ln(x) - \mu}{\beta}\right) \tag{1}$$

where $P(C|IM = x)$ is the probability that a ground motion record with $IM = x$ will cause the structure to collapse or exceed a certain limit of the maximum inter-story drift ratio (IDR), $\Phi(\cdot)$ is the standard normal probability integral CDF, μ and β are the logarithmic median and the standard deviation of $\ln IM$. The construction of fragility functions is a process of estimating μ and β for Eq. (1).

For any new structural system, such as balloon-framed CLT construction, for which there are no past damage data from earthquakes, performing NLTHA is the most feasible approach in earthquake engineering for deriving fragility functions. The developed functions are so-called analytical fragility functions, as one needs to decide the *IM* levels at which to perform the analyses.

A common method to estimate parameters for a fragility function is IDA (Vamvatsikos and Cornell 2002). In conventional IDA, the computational demand is high, as some records may need significant scaling to cause collapse. The large-*IM* results (up to 5–6 times of the design earthquake intensity) are questionable and of little interest to the engineering practice. To address these issues, in a truncated IDA, the analysis is performed only up to an upper bound intensity, $IM_{\max}$ (Baker 2015).

One important output from IDA is the collapse margin ratio (CMR) (FEMA 2009), defined as the ratio between median collapse intensity, S_{CT}, and the maximum considered earthquake intensity in US code (equivalent to the 2% in 50 years uniform hazard spectrum level in Canadian code), S_{MT}.

$$CMR\, =\, \frac{S_{CT}}{S_{MT}} \tag{2}$$

An accurate structural model that represents the nonlinear building behavior and simulates its collapse state at large deformation is essential for IDA. To achieve this, component models must capture degradation in strength and stiffness, both cyclic and in-cycle, and be calibrated with test data.

To account for uncertainties associated with modeling and record selection, FEMA P695 (FEMA 2009) introduced four parameters, namely the record-to-record uncertainty β_{RTR}, design requirements uncertainty β_{DR}, test data uncertainty β_{TD}, and modeling uncertainty β_{MDL}, to derive the total system collapse uncertainty β_{OT} as

$$\beta_{TOT} = \sqrt{\beta_{RTR}^2 + \beta_{DR}^2 + \beta_{TD}^2 + \beta_{MDL}^2} \tag{3}$$

This approach, well-established in earthquake engineering and adopted for evaluating the collapse capacity of several timber hybrid buildings (Bezabeh et al. 2017; Koliou et al. 2016; Kovacs and Wiebe 2019; Luo et al. 2022; Shahnewaz et al. 2020; Tesfamariam et al. 2021; van de Lindt et al. 2020), was selected to analyze the balloon-framed CLT structure of the Begbie school building.

2. Building Description

The Begbie Elementary School building consists of a northern classroom block, and a southern classroom and gymnasium block. To simplify the balloon-frame analysis without adding the complexity of the gymnasiums, this study focused on the northern block, which has a dimension of 25.5 m (North-South) by 35.1 m (East-West), see Fig. 1.

The story heights for the first and second floor are 4.35 and 4.0 m, respectively. The CLT walls have two different thicknesses: 139 and 191 mm, both strength grade V2.1 (CSA 2019). The walls are balloon-framed with ledgers to support the second floor. The building was designed for a live load of 2.4 kPa and a superimposed dead load of 2.5 kPa that includes non-structural topping, partitions, and finishes. The seismic design of the building was based on the 2015 National Building Code of Canada (NBCC) (NBCC 2015) for Site Class C (very dense soil). A high important factor I_{E} of 1.3 was applied, with seismic ductility and overstrength reduction factors R_{d} of 2.0 and R_{o} of 1.5, respectively. These reduction factors correspond to the code prescribed factors for platform framed CLT shear walls;

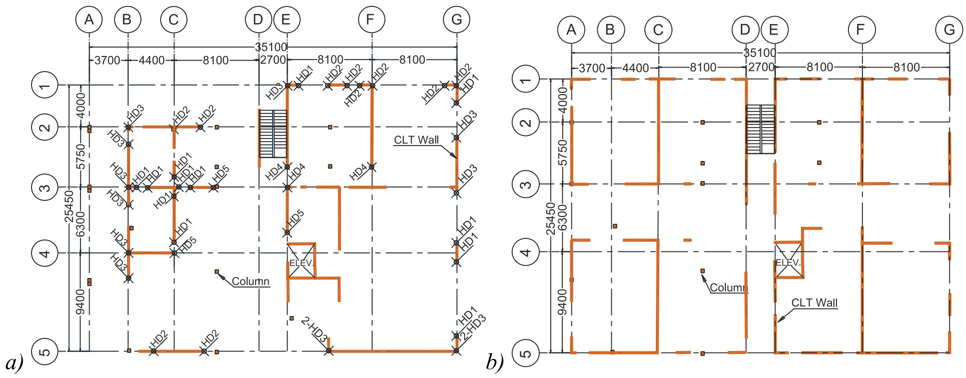

Figure 1. Floor plans of the northern block: (a) level 1 and (b) level 2 (unit: mm).

Table 1. HD and spline connections.

Mark	Type	Fasteners	
HD1	WHT440	30 Ø4 × 60 mm nails	
HD2	WHT620	55 Ø4 × 60 mm nails	
HD3	WHT740	75 Ø4 × 60 mm nails	
HD4	Custom	Six Ø12 mm stainless steel tight-fit pins	
HD5	Custom	Ten Ø12 mm stainless steel tight-fit pins	
Mark	Type	Fasteners #1	Fastener #2
SP1	Plywood spline	Ø8 × 120 mm screws @ 600 mm	Ø4 × 60 mm nails @ 250 mm
SP2	Plywood spline	Ø8 × 120 mm screws @ 600 mm	Ø4 × 60 mm nails @ 200 mm
SP3	Plywood spline	Ø8 × 120 mm screws @ 600 mm	Ø4 × 60 mm nails @ 150 mm
SP7	Half-lap joint	Ø8 × 140 mm screws @ 250 mm	-
SP8	Half-lap joint	Ø8 × 120 mm screws @ 200 mm	-
SP9	Half-lap joint	Ø8 × 120 mm screws @ 600 mm	-
SP11	Half-lap with steel plate	2 rows of Ø8 × 120 mm screws @ 200 mm	-

based on the physical testing reported by Shahnewaz, Dickof, and Tannert (2021) the designers were confident in using these factors for this balloon-framed structure.

The CLT walls were detailed with capacity protected WB connections. Notched glulam sill plates were anchored on the concrete footing to support the wall panels with Ø10 × 140 mm partially threaded screws with washer heads (PSW) spaced at 65–300 mm. HDs and SPs were designed as the dissipative elements; there were 11 types of HDs and 12 types of SPs in the whole building. Among them, five types of HDs and seven types of SPs were used in the northern block, as summarized in Table 1. HD1 to HD3 are WHT angle plates with different numbers of anker nails, while HD4 and HD5 are made of 13 mm thick customized stainless steel internal plates installed with Ø12 mm tight fit pins. SP1 to SP3 are provided with 25 × 140 mm D.Fir plywood surface-splines mounted with 2 types of fasteners (PSW and smooth shank nails) at different spacings. SP7 to SP9 are 80 mm half-lap joints combined with partially threaded screws with hex heads (PSH). SP11 was a 200 mm half lap joint combined with a steel connector plate, which was used for corners of openings with two rows of PSH. The connection layout of a typical Gridline G is illustrated in Fig. 2a and b shows the wall assembly at the construction site.

Figure 2. Balloon-framed shear walls: (a) elevation view of Grid G and (b) construction site photo.

3. Numerical Modeling

3.1. Modeling Development

The nonlinear 3D model of the building's northern block, shown in Fig. 3a, was developed in OpenSees (Mazzoni et al. 2006). Shell elements were used for the CLT wall panels, and nonlinear springs were used for the wall-to-foundation and wall-to-wall connections. An isotropic elastic

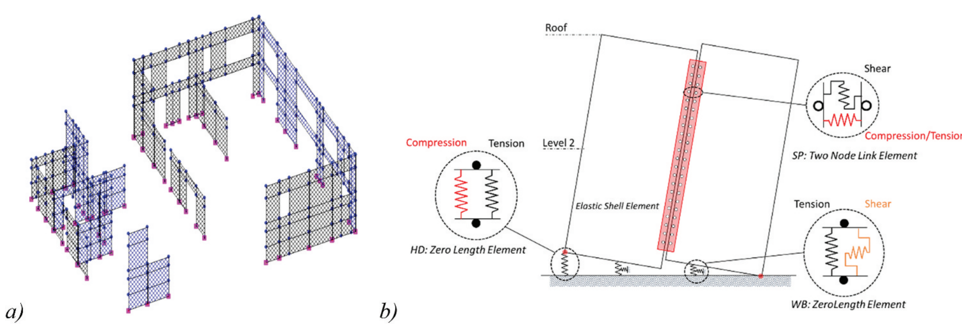

Figure 3. OpenSees model of the school building: (a) 3D sketch and (b) 2D coupled shear wall.

material was adopted for the shellMITC4 element to model the CLT panels as the nonlinearity of CLT shear walls is concentrated at the connections (Rinaldin and Fragiacomo 2016). Two types of non-linear spring elements were used to model the connections: (1) HD and WB were modeled with zeroLength element and (2) SP were modeled with twoNodeLink elements, both with independent behavior along three local axes (tension, shear, and out-of-plane). The ledgers were excluded as they were shown to have minimal impact on the lateral behavior of the balloon-frame system (Shahnewaz, Dickof, and Tannert 2021). Based on previous experimental and numerical studies (Furley et al. 2021; Miller et al. 2021; Popovski, Gavric, and Schneider 2014), the floor and the roof were modeled as rigid diaphragms with mass lumped at each story. The first two fundamental periods of the nonlinear building model at both translational directions were determined as 0.46 s and 0.44 s. The first mode is predominately in the E-W direction and the second mode is in the N-S direction, indicating the northern block of the school building is stiffer in the N-S direction.

Figure 3b illustrates the modeling schematic of a typical coupled balloon-framed CLT shear wall with three non-linear connections. The nonlinear Pinching4 material model was implemented in OpenSees and calibrated with experimental data to account for the nonlinear behavior of connections at large deformations, including pinching and degradation in stiffness and strength. The Pinching4 model, shown in Fig. 4a, has a piecewise linear backbone curve controlled by 16 parameters with additional 6 pinching parameters and 17 degradation parameters. The detailed calibration process will be presented subsequently.

The HDs resist uplift only, so each HD was assigned with one Pinching4 model in the vertical direction. To simulate the contact compression behavior at panel edge, an elastic-no-tension (ENT) material model (see Fig. 4b) with large compression stiffness was introduced in parallel with the tension spring of the HD; the compression stiffness for the ENT model was taken as 1,500 MPa as suggested by Sun et al. (2018). No shear resistance was considered for the HD.

The WB connections were modeled using two orthogonal springs to simulate both tension and shear resistances. It has been reported that conventional wall base angle bracket connections have similar strength in both directions (Masroor, Doudak, and Casagrande 2020; Shahnewaz et al. 2020), so the same Pinching4 parameters were used for both directions. For computational efficiency, the WBs are simplified as a single zeroLength element for each wall panel; the assigned properties represent the combined capacity of all the equally spaced screws at that panel (panel length divided by the spacing). The SP connections use the same procedure as the WBs at each story, one twoNodeLink element assigned at the mid-height of each story represent all the fasteners in the SP connections. Pinching4 material properties were assigned in the shear direction of the link element as the SP connections act to resist shear force only. A horizontal spring with the ENT material in parallel with an elastic tension stiffness was assigned to model the contact between adjacent panels. It is worth mentioning that the two types of fasteners at different spacings provided for SP1-3 are modeled with parallel material models to combine both calibrated Pinching4 materials each fastener type, as shown in Fig. 5.

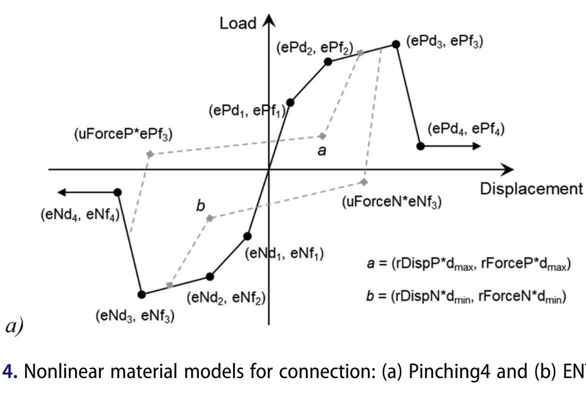

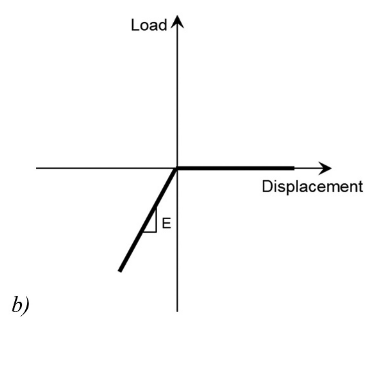

Figure 4. Nonlinear material models for connection: (a) Pinching4 and (b) ENT.

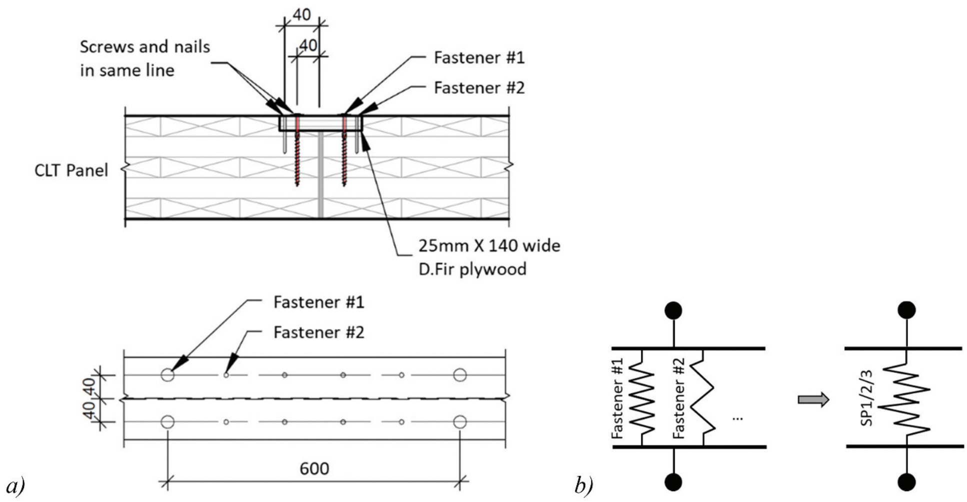

Figure 5. Fasteners in SP1/2/3: (a) joint layout and (b) parallel material model.

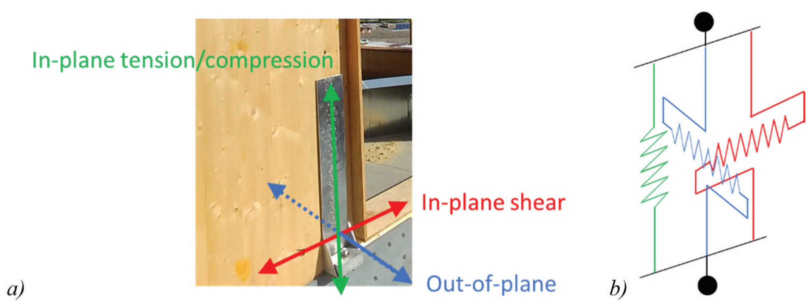

Figure 6. Connection modeling: (a) in- and out-of-plane behavior and (b) 3D spring element.

Unlike 2D modeling, the connections in a 3D model will experience multi-directional forces under both in- and out-of-plane lateral loads. To account for this effect, an out-of-plane spring perpendicular to the wall plane was introduced for each zeroLength element of connections, as shown in Fig. 6. As limited experimental data are available for the connection subjected to the out-of-plane loading, a linear elastic material model that has the same stiffness of the in-plane shear was assigned for the out-of-plane spring, as suggested by Rinaldin and Fragiacomo (2016). For modeling the orthogonal wall-to-wall connections at a corner, a link element with a linear elastic material stiffness of 60,000 kN/m to represent the partially threaded screws with countersunk heads (PSC) Ø8 × 180 mm screws was implemented in the vertical shear direction; linear material properties with very high stiffness were implemented for the in-plane tension and out-of-plane directions.

3.2. Model Calibration and Validation

In a first step, the pinching4 hysteresis parameters for each connection (HD, WB, and SP) were calibrated with experimental data available form from UNBC tests or from the literature. In a second step, the calibrated connection models were validated by simulating the nonlinear response of a full-scale balloon-framed CLT shear wall tested under reversed cyclic loading at UNBC.

Since the tested specimens had different number of fasteners than the connections designed for the building, the calibration was first conducted for a single fastener and then linearly scaled based on the number of the fasteners with the same deformation capacity. It has been reported that the strength of steel connections in timber construction is approximately linear-proportional to the number of the fasteners and this simplification has been widely used and accepted for connection modeling (Gavric, Fragiacomo, and Ceccotti 2015b; Shahnewaz, Popovski, and Tannert 2019).

Reversed cyclic tests conducted at UNBC for two HD types, WHT440 and WHT740, were used for calibrating the HD1-3. More specifically, the WHT440 test with 15 Ø4 × 60 mm nails was used to calibrate HD1 (WHT440), while the WHT740 test with 38 Ø4 × 60 mm nails was used to calibrate both HD2 (WHT620) and HD3 (WHT740). Figure 7a and b present the tested load–displacement hysteresis curves for both HDs and the calibrated Pinching4 models for each. The calibrated Pinching4 model simulated the nonlinear behavior of the HDs well in terms of the peak capacity, unloading and reloading stiffness, and the pinching effect. The large negative stiffness due to contact compression was captured with the ENT model. (Note: HD4/5 and SP11 around corners of openings were capacity-protected to remain elastic and were modeled as linear elastic.)

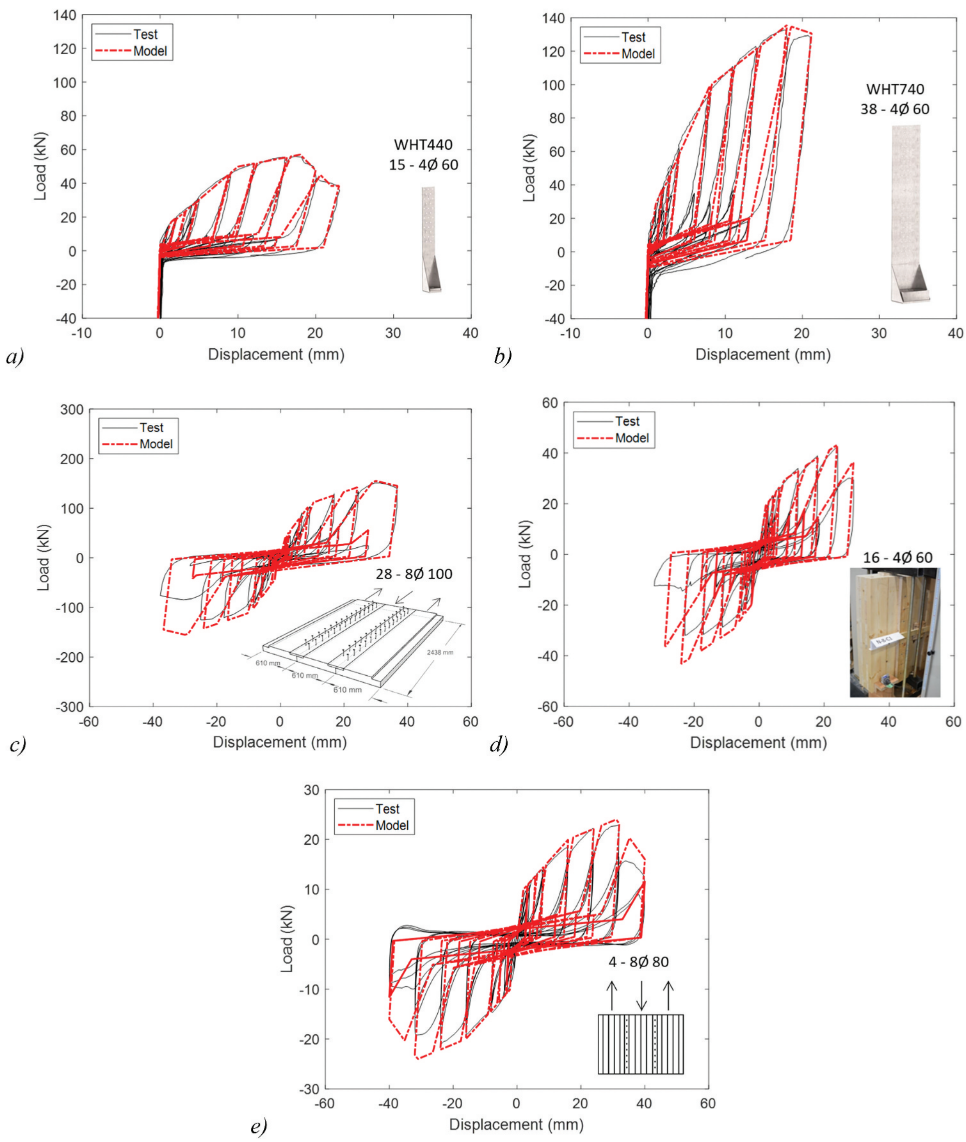

Figure 7. Hysteresis calibration of connections: (a) HD1; (b) HD2-3; (c) fastener #1 in SP1-3; (d) fastener #2 in SP1-3; (e) SP7-9.

For SP1-3 with two types of fasteners, test data from two sources were used: fastener #1 (PSW 8Ø 120) was configured using spline connection tests with Ø8 × 100 mm screws conducted by Sullivan, Miller, and Gupta (2018), and fastener #2 (shank nails Ø8 × 120 mm) was calibrated with component level tests conducted at UNBC. The hysteretic test and model behaviour for individual screws and nails are shown in Fig. 7c and d, respectively. The numerical model slightly overestimated the capacity at the negative phase due to the asymmetric performance of the spline test. Both calibrated Pinching4 models were combined through the parallel material as mentioned in the previous section. The half-lap joint connections SP7-9 were calibrated based on test data using Ø8 × 80 mm screws with 50 mm overlap length from Gavric, Fragiacomo, and Ceccotti (2015a), as seen in Fig. 7e. As the length of the screw in the tests was smaller than those used in SP7-9 (Ø8 × 120/140 mm), the calibrated backbone curve was scaled up by 60% based on the screw resistance ratio estimated as per Clause 12.6 in CSA O86 (CSA 2019).

The calibrated parameters for the Pinching4 material model for each connection can be found in Appendix. It should be noted that since there are no test data available for the designed WB connections, a simplification was made that the elastic region of the Pinching4 model was determined with design resistance of the WB connections (3.8 kN per screw) whose post-yielding and hysteresis parameters were calibrated with cyclic test data of a TCN240 angle bracket.

Before completing the building model, the calibrated connection models were validated by simulating the nonlinear response of a full-scale balloon-framed CLT shear wall tested under reversed cyclic loading. The test specimen consisted of two coupled CLT panels with a dimension of 1,219 mm by 3,658 mm, representing a half-scale two-story wall, as shown in Fig. 8. The same HD3 and SP2 were used for the wall-to-foundation and wall-to-wall connections and four TCN240 angle bracket were used, see Shahnewaz, Dickof, and Tannert (2021).

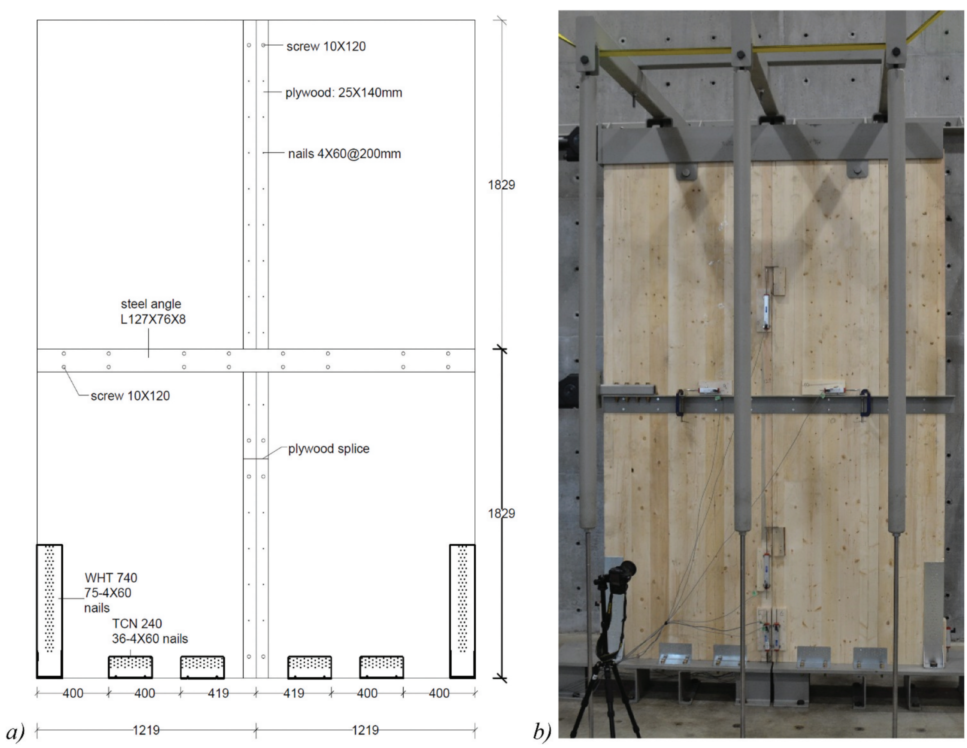

Figure 8. Balloon-framed shear wall test specimen: (a) schematic and (b) photo.

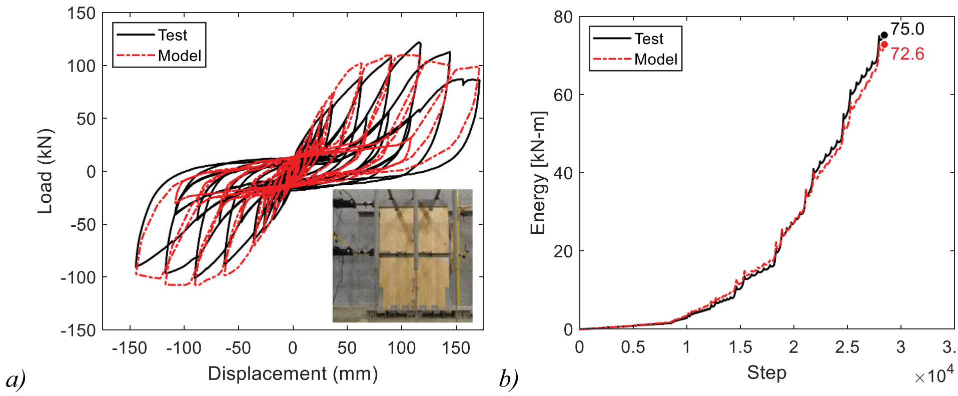

Figure 9. Shear wall test versus model: (a) hysteresis curve and (b) cumulative energy.

A comparison between the predicted load–displacement hysteresis curve from the numerical model and the actual test results showed good agreement, see Fig. 9a. The model simulated both the initial stiffness, peak capacity, and the nonlinear behavior (e.g. the pinching effect and the degradation) of the wall test with reasonable accuracy. The differences in both initial stiffness and peak load between the model and the test were less than 10%. Dissipated cumulative energy was also compared, the model predicted the energy very well throughout the entire reversed cyclic loading with 3% difference when compared to the test, see Fig. 9b. These results validated the modeling approach; thus, the model was deemed adequate for the seismic assessment of the two-story building.

4. Ground Motion Selection

4.1. Cascadia Subduction Zone

To perform NLTHA and IDA on a 3D model, appropriate bi-directional ground motion records that represent the characteristic seismicity of the location need to be selected. The building site, Vancouver, BC, is located in an active seismic region, called the Cascadia Subduction Zone (Pan, Ventura, and Tannert 2020). The local seismicity is dominated by the subduction of the Juan de Fuca plate beneath the continental North American plate. The earthquake hazard is contributed by three sources: (1) shallow crustal earthquakes within the crust of the North American plate; (2) subduction inslab earthquakes within the sinking Juan de Fuca plate; and (3) subduction interface earthquakes at the interface of two plates (Adams et al. 2015).

4.2. Probabilistic Seismic Hazard Analysis

A probabilistic seismic hazard analysis (PSHA) was conducted to evaluate the seismic hazard of the region. PSHA takes the possible seismic sources near the site location and evaluates the probability based on the return period for different shaking intensities and magnitude (Baker 2008). It identifies the sources where the earthquake may come from and characterizes how the earthquake magnitude and distance are distributed. This process is also known as seismic hazard deaggregation (Kramer 1996). The analysis was based on Canada's fifth generation seismic hazard model (Adams et al. 2015). Figure 10 shows the seismic deaggregation for Vancouver (Class C) for a return period of 2475 years (a 2% probability of exceedance in 50 years) at the spectral acceleration of the building period. The seismic hazard is broken into its contributions by magnitude (M_w), distance, and earthquake type. The site is dominated by the subduction inslab earthquake with a contribution of 69% to the total hazard, following by the subduction interface and crustal earthquakes with contributions of 16% and 15%, respectively. The mean magnitude and distance for each earthquake type is summarized in Table 2.

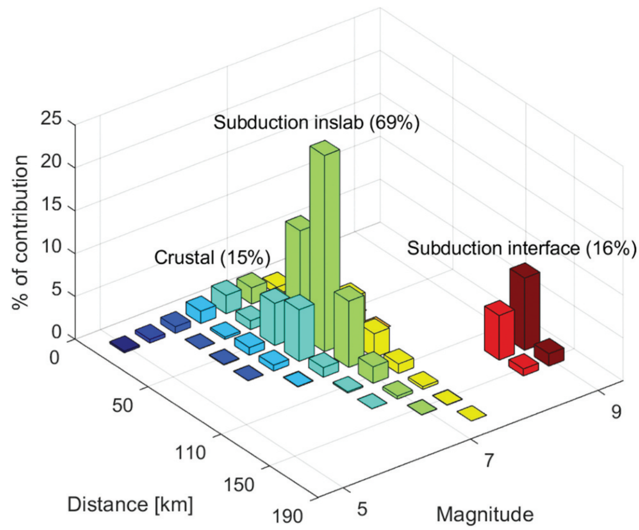

Figure 10. Seismic deaggregation for Vancouver at building period.

Table 2. Deaggregation results.

Mean scenario	Crustal	Subduction inslab	Subduction interface
Magnitude	6.8	7.0	8.9
Distance (km)	22.9	70.6	134.0
Contribution	15%	69%	16%

4.3. Ground Motions Selection and Scaling

The ground motion selection of the NBCC for dynamic analysis is a targeted process, requiring an ensemble containing at least 11 motions whose response spectra were matched to the target design spectrum. When two or more seismic scenarios are considered (e.g. Vancouver in BC), a minimum of five motions must be selected for each. To be more conservative, based on the PSHA results, seven historical ground motion records (two horizontal components for each record) were selected from earthquake database for each earthquake type: the PEER NGA-West 2 database (PEER 2013) was used to retrieve crustal records, while the seven subduction inslab and seven interface records were selected from the K-NET/KiK-net (K-net 2012) and COSMOS (COSMOS 2011) databases. In accordance with the 2015 NBCC, all 21 records, listed in Table 3, were linearly scaled to match the target uniform hazard spectrum (UHS) for the Vancouver site with Class C over a period range of 0.2–2.0 *T*, where *T* is the building's fundamental period. The same scaling factor (SF) was applied for both horizontal components. Figure 11 shows the response spectra of all selected motions and their mean spectrum matched to the Vancouver UHS.

5. Results and Discussion

5.1. Nonlinear Time History Analysis at Design Level

Figure 12a shows the *IDR*s of the modeled building for each ground motion and the mean value of all *IDR*s. The average of the maximum *IDR*s was 0.51% at the first story for both directions, 2% drift limit specified in NBCC for a high importance building. Subduction inslab motions were found to generate the largest *IDR* (0.56%) at the primary E-W direction, 21% and 10% higher than those from the crustal and subduction interface motions, respectively. The same trend was observed for the story

Table 3. Information of selected ground motions.

Type	No.	Event	Year	M_w	Distance (km)	Station	SF
Crustal	1	San Fernando (US)	1971	6.6	22.6	Castaic – Old Ridge	0.94
	2	Imperial Valley (US)	1979	6.5	15.2	Cerro Prieto	1.20
	3	Irpinia (Italy)	1980	6.9	30.1	Rionero In Vulture	2.31
	4	Loma Prieta (US)	1989	6.9	20.3	Anderson Dam	3.73
	5	Chuetsu-oki (Japan)	2007	6.8	25.5	Joetsu Yasuzukaku	1.15
	6	Iwate (Japan)	2008	6.9	36.3	Sanbongi Osaki City	2.14
	7	Iwate (Japan)	2008	6.9	22.4	Yuzawa Town	1.34
Subduction Inslab	1	Geiyo (Japan)	2001	6.4	59.3	Towa	0.97
	2	Geiyo (Japan)	2001	6.4	56.4	Matsuyama	0.94
	3	Geiyo (Japan)	2001	6.4	59.9	Kawauchi	2.27
	4	Michoacan (Mexico)	1997	7.1	89.4	Villita	3.14
	5	Michoacan (Mexico)	1997	7.1	110.4	La Union	4.63
	6	Nisqually (US)	2001	6.8	71.3	Seattle Fire Stat	4.97
	7	Nisqually (US)	2001	6.8	59.3	Gig Harbor Fire Stat	2.73
Subduction Interface	1	Tohoku (Japan)	2011	9.0	89.5	Toyosato	0.54
	2	Tohoku (Japan)	2011	9.0	170.8	Shimoyachi	4.63
	3	Tohoku (Japan)	2011	9.0	111.3	Taiwa	0.70
	4	Michoacan (Mexico)	1985	8.1	38.3	Caleta De Campos	1.75
	5	Maule (Chile)	2010	8.8	136.0	Hualane	0.59
	6	Hokkaido (Japan)	2003	8.3	148.4	Kawayu	3.18
	7	Hokkaido (Japan)	2003	8.0	160.9	Oiwake	2.16

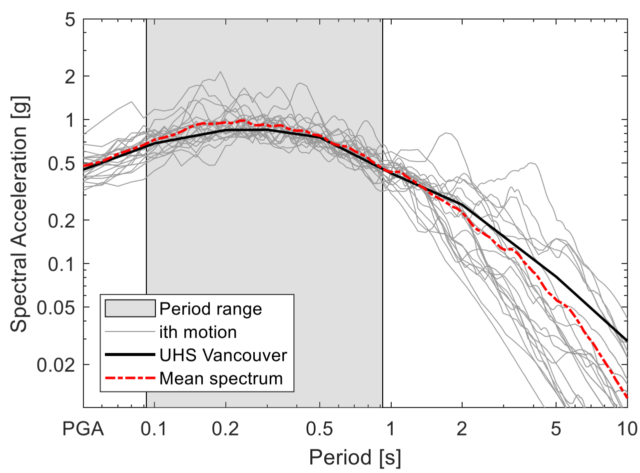

Figure 11. Response spectra of selected motions matched to the target spectrum.

displacement. Figure 12b shows the average of the maximum roof displacements was 38 and 32 mm for the E-W and N-S directions, the largest displacement observed (59 mm) was similarly from one subduction inslab motion – the Geyio earthquake (No. 1) in the E-W direction.

Figure 13 shows the maximum base shear forces observed for each ground motion. The average BS for E-W and N-S directions was 1501 and 1509 kN, respectively, 4% lower than that calculated from the equivalent static force procedure (1563 kN) in design as per (NBCC 2015).

Global hysteresis curves (roof displacement vs. base shear) of the building subjected to three selected ground motions from each earthquake type are presented in Fig. 14. The building dissipated earthquake energy through hysteretic nonlinear behavior of the connections (pinching and degradation); the wall-to-wall spine joints showed the majority of the dissipation, as intended in the design. As expected, the building model did not show any significant torsional effect as this low-rise school building was designed with shear walls at its perimeter.

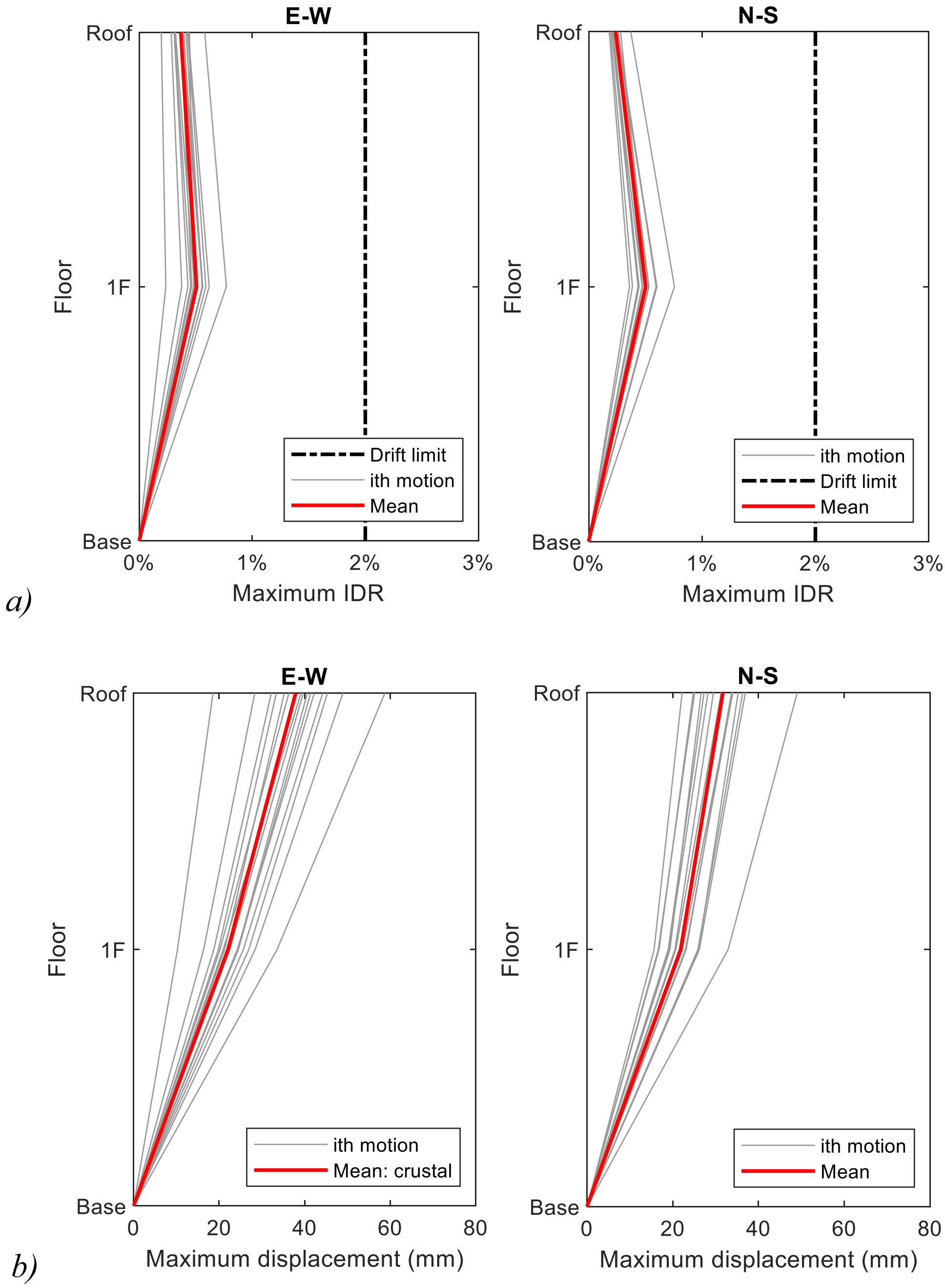

Figure 12. Maximum responses at design intensity level: (a) IDR and (b) story displacement.

Figure 15 shows the localized nonlinear hysteresis response of representative SPs, including SP1 at grid 5 F and SP8 at grid 3C-D, and SP7 at grid E1-2 and SP2 at grid B2-3 (Fig. 1). For brevity, only the responses when subjected to the Michoacan subduction interface record (No. 4) were plotted. All the SPs exhibited nonlinear response and started to dissipate energy with relative slips were less than 20 mm with shear forces ranging from 50 to 80 kN. The HDs remained in the elastic range with an uplift displacement ranging from 2 to 10 mm. Figure 16 shows the average of the maximum uplift forces of

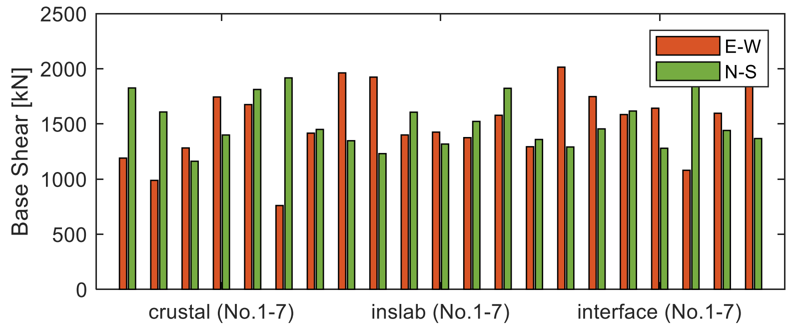

Figure 13. Maximum base shear at design level.

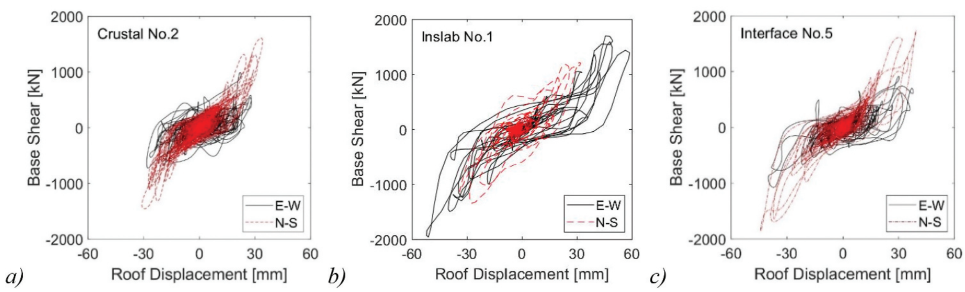

Figure 14. Global hysteresis curves of selected motions at design level: (a) crustal No. 2; (b) subduction inslab No. 1; and (c) subduction interface No. 5.

the HDs for the balloon-frame shear walls when subjected to the 21 motions. For the long balloon-framed shear walls with openings, such as at Grid locations 5C, 5 F, and E2, the uplift forces for HD2 and HD3 were as high as 82–97 kN. The peak of 133 kN was obtained from the linear HD5 with high stiffness at Grid 3 CD.

5.2. Incremental Dynamic Analysis

IDA was performed for each bidirectional ground motion pair scaled from 20% to 400% ($IM_{\max}$) of the UHS design intensity with a 20% increment. In total, 420 NLTHA (3 sets of 7 motions at 20 intensity levels) were conducted. For the 3D model, the maximum inter-story drift ($IDR_{\max}$) of the building was monitored, which was taken as the square root of the *IDR* at both E-W and N-S directions (Sun et al. 2018):

$$IDR_{max} = \sqrt{IDR_{EW,max}^2 + IDR_{NS,max}^2} \tag{4}$$

Figure 17 shows the *IDA* curves of the building model subjected to 21 ground motions of varying intensities and their median value.

Considering a 7% IDR to be a reasonable collapse criterion based on FEMA P695 and studies on wood and CLT structures (Ho et al. 2017; Kovacs and Wiebe 2019), each black dot on the curve represents the onset intensity of collapse (i.e. next intensity level will exceed the limit). At the design intensity level (100% of UHS), the maximum drifts were less than 1%. With the increasing intensity, the building model started to collapse under the crustal (No. 4) Loma Prieta motion at 220% UHS and the subduction interface (No. 4) Michoacan motion at 240% of UHS, respectively. The largest drift before the collapse was monitored as 6.5% when subjected to the crustal (No. 7) Iwate motion at 300% of UHS.

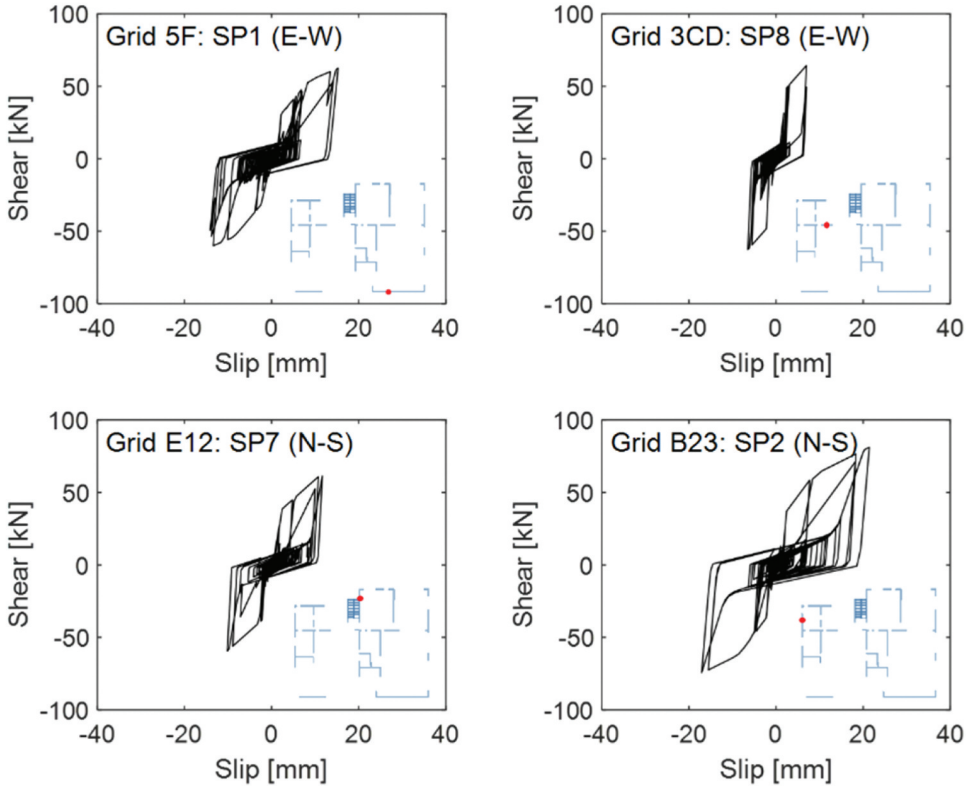

Figure 15. Hysteresis curves of representative SP connections at design level (subduction interface No. 4).

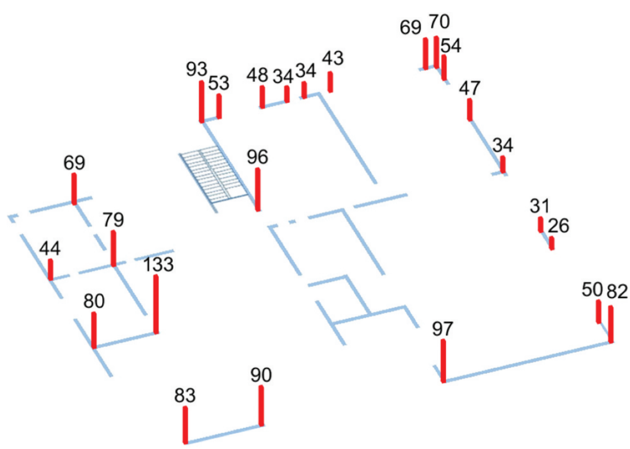

Figure 16. Maximum uplift forces (kN) in HDs at design level.

5.3. Fragility Assessment

Based on the *IDA*, the collapse fragility curve was developed, see Fig. 18. The red line is the CDF by fitting a lognormal distribution through the empirical collapse data points (black dots) (Baker 2015). The median collapse capacity (50% probability of collapse) was determined at *IM* of S_{CT} = 2.41 g (i.e.

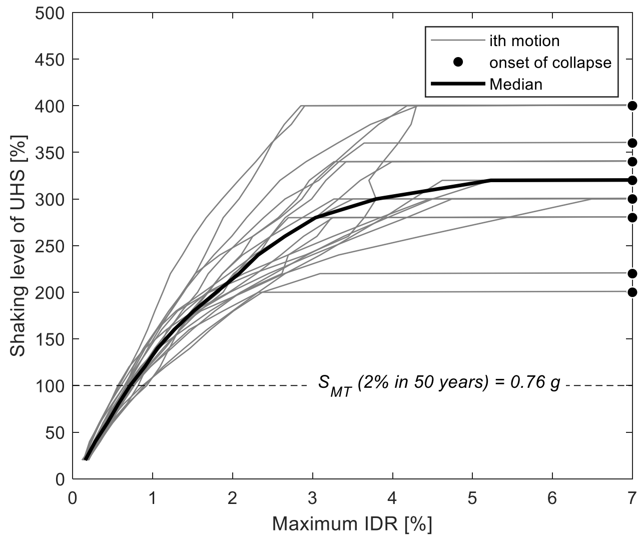

Figure 17. IDA curves of all ground motions.

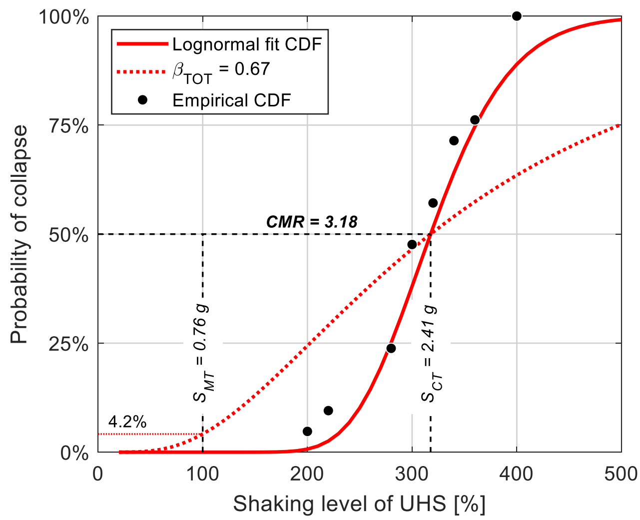

Figure 18. Fragility curve for collapse with uncertainty.

320% of UHS). Considering the design intensity of S_{MT} = 0.76 g, the CMR was calculated as 3.18 for the Begbie School building model.

Subsequently, the fragility curve with the uncertainties was developed. Based on the quality rating for each variability specified in FEMA P695, a β_{DR} of 0.35 was used as a "fair" design with a medium level of confidence on the basis of design requirements and a medium level of completeness and robustness. Based on the sufficient testing conducted at laboratory on both connections and shear walls, the test data was rated as "good" with a β_{TD} of 0.2. The numerical model was rated as "fair" with a β_{TD} of 0.35 since it covered most of the design space and was validated with cyclic test data at large deformation. By considering a conservative record-to-record variability β_{RTR} of 0.4, the total uncertainty β_{TOT} of 0.67 was calculated. As shown in the red dash line in Fig. 18, the building had 4.2% probability of collapse at the 2% in 50 years design level, meeting the requirement of less than 10% according to FEMA P695. According to FEMA P695, acceptable structural performance for an

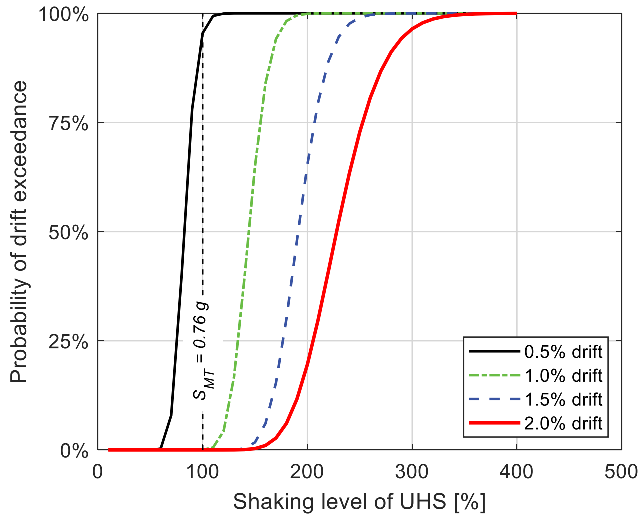

Figure 19. Fragility curves for drift exceedance.

individual building archetype is achieved if the adjusted collapse margin ratio (ACMR) exceeds $ACMR_{20\%}$, defined as the ACMR for the 20% collapse probability based on the β_{TOT}. The ACMR can be calculated as the product of CMR and spectral shape factor. However, according to Tesfamariam et al. (2021), this factor does not apply for a site-specific hazard and therefore, the same CMR value was applied to the ACMR. Based on Table 7–3 of FEMA P695, for a total uncertainty β_{TOT} of 0.67, the $ACMR_{20\%}$ criterion is 1.76, which is lower than the ACMR of 3.18, indicating the building satisfied the criterion.

Although this study was focused on a balloon-framed building, it was deemed useful to indirectly compare its performance to that of platform-type CLT buildings. Shahnewaz et al. (2020) estimated the CMR for a four-story platform-type building as 2.78–3.55 at collapse drifts ranging from 5% to 10%, with a probability of collapse of 4.1% to 8.1% for a β_{TOT} of 0.73. Kovacs and Wiebe (2019) calculated collapse probabilities ranging from 9.2% to 11.7% for three- to nine-story buildings at the maximum considered earthquake level (equivalent to the UHS level in Canada). Similarly, van de Lindt et al. (2020) conducted seismic performance of 72 platform-type CLT archetype buildings for US hazards and observed probabilities of collapse of up to 15% considering the total uncertainty. The balloon-framed building studied herein exhibited a lower a probability of collapse than those platform-type buildings. However, different modeling approaches were applied and the buildings were subjected to different seismic hazards; therefore, no direct comparison is possible.

Fragility curves for drift exceedance were also derived for various drift limits of 0.5%, 1.0%, 1.5%, and 2.0%, as shown in Fig. 19. At the design intensity level, the probability of exceeding 0.5% drift was 95%, but was 0% for exceeding higher drift limits. The median probability of drift exceedances for each drift limit was at 83%, 144%, 191%, and 228% of the UHS level.

6. Conclusions

This study investigated the seismic performance and collapse capacity of an actual two-story CLT balloon-framed school building. NLTHA of selected motions at the design earthquake level (2% in 50 years) was conducted. Subsequently, IDA was performed to derive fragility curves for collapse capacity and drift exceedance. Based on the analysis results, the building model (northern block) met the seismic design criterion for Vancouver, BC, Canada with the maximum drift below the 2% limit for a 2475-year return period earthquake hazard. A very low 4.2% probability of collapse was estimated for the building at the design level taking all uncertainties into account per FEMA P695. The building had a 50% probability of exceeding the 2% drift limit and a 50% probability of collapse when the ground intensity increased to 228% and 320% of the design level, respectively. The results confirmed that the use of the seismic reduction factors in Canadian code defined for the platform-type CLT shear walls in the design of a balloon-framed CLT shear wall system provided adequate seismic resistance.

Interpretation of these results must recognize the assumptions and simplifications. The collapse risk at high intensity level may be affected by modeling simplifications of several connections (e.g. HD4/5 and SP11) due to the lack of test data. The out-of-plane responses of 3D connections were simplified as linear elastic. The verification for the modeling approach was carried out with reversed cyclic loading test only, no actual shake table test data were available at the current stage to validate the nonlinear numerical model under dynamic loading. Future experimental research on these issues should be undertaken to further validate the accuracy of the numerical modeling of balloon framed CLT building, especially for potential high-rise construction.

Acknowledgments

The project was supported by Natural Resources Canada (NRCAN) through the Green Construction Wood (GCWood) program and by the Government of Canada through a Canada Research Chair.

Disclosure Statement

No potential conflict of interest was reported by the author(s).

Funding

This work was supported by the Canada Research Chair in Hybrid Wood Structures Engineering [950-231286] and Natural Resources Canada [GCW-LRNR19].

ORCID

Yuxin Pan http://orcid.org/0000-0002-6015-0110

References

Adams, J., S. Halchuk, T. Allen, and G. Rogers 2015. "Canada's 5th generation seismic hazard model, as prepared for the 2015 National Building Code of Canada." In *Proc., 11th Canadian Conference on Earthquake Engineering*, 21–24. Victoria, BC, Canada.

Baker, J. W. 2008. "An introduction to probabilistic seismic hazard analysis (PSHA), White Paper Version 2.1." 77 pp.

Baker, J. W. 2015. Efficient analytical fragility function fitting using dynamic structural analysis. *Earthquake Spectra* 31 (1): 579–99. doi: 10.1193/021113EQS025M.

Bezabeh, M., S. Tesfamariam, M. Popovski, K. Goda, and S. Stiemer. 2017. Seismic base shear modification factors for timber-steel hybrid structure: Collapse risk assessment approach. *Journal of Structural Engineering* 143 (10): 04017136. doi: 10.1061/(ASCE)ST.1943-541X.0001869.

Brandner, R., G. Flatscher, A. Ringhofer, G. Schickhofer, and A. Thiel. 2016. Cross laminated timber (CLT): Overview and development. *European Journal of Wood and Wood Products* 74 (3): 331–51. doi: 10.1007/s00107-015-0999-5.

Ceccotti, A., C. Sandhaas, M. Okabe, M. Yasumura, C. Minowa, and N. Kawai. 2013. SOFIE project–3D shaking table test on a seven-storey full-scale cross-laminated timber building. *Earthquake Engineering & Structural Dynamics* 42 (13): 2003–21. doi: 10.1002/eqe.2309.

Chen, Z., and M. Popovski. 2020. Mechanics-based analytical models for balloon-type cross-laminated timber (CLT) shear walls under lateral loads. *Engineering Structures* 208: 109916. doi: 10.1016/j.engstruct.2019.109916.

COSMOS. 2011 October. "*Global component of the center for earthquake strong motion data, strong-motion virtual data center*." https://strongmotioncenter.org/vdc/scripts/default.plx

CSA. 2019. *CSA O86-19 engineering design in wood, Canadian standard association*. Mississauga, Canada: CSA Group.

FEMA. 2009. *Quantification of building seismic performance factors, Federal Emergency Management Agency (FEMA), P695*. Washington, DC: Federal Emergency Management Agency.

Flatscher, G., K. Bratulic, and G. Schickhofer. 2015. Experimental tests on cross-laminated timber joints and walls. *Proceedings of the Institution of Civil Engineers-Structures and Buildings* 168 (11): 868–77. doi: 10.1680/stbu.13.00085.

Furley, J., J. W. van de Lindt, S. Pei, S. Wichman, H. Hasani, J. W. Berman, K. Ryan, J. Daniel Dolan, R. B. Zimmerman, and E. McDonnell. 2021. Time-to-functionality fragilities for performance assessment of buildings. *Journal of Structural Engineering* 147 (12): 04021217. doi: 10.1061/(ASCE)ST.1943-541X.0003195.

Gavric, I., M. Fragiacomo, and A. Ceccotti. 2015a. Cyclic behavior of CLT wall systems: Experimental tests and analytical prediction models. *Journal of Structural Engineering* 141 (11): 04015034. doi: 10.1061/(ASCE)ST.1943-541X.0001246.

Gavric, I., M. Fragiacomo, and A. Ceccotti. 2015b. Cyclic behavior of typical screwed connections for cross-laminated (CLT) structures. *European Journal of Wood and Wood Products* 73 (2): 179–91. doi: 10.1007/s00107-014-0877-6.

Ho, T. X., T. N. Dao, S. Aaleti, J. W. van de Lindt, and D. R. Rammer. 2017. Hybrid system of unbonded post-tensioned CLT panels and light-frame wood shear walls. *Journal of Structural Engineering* 143 (2): 04016171. doi: 10.1061/(ASCE)ST.1943-541X.0001665.

Ibarra, L. F., and H. Krawinkler. 2005. *Global collapse of frame structures under seismic excitations*. Berkeley, CA: Pacific Earthquake Engineering Research (PEER) Center ".

Jalilifar, E., M. Koliou, and W. Pang. 2021. Experimental and numerical characterization of monotonic and cyclic performance of cross-laminated timber dowel-type connections. *Journal of Structural Engineering* 147 (7): 04021102. doi: 10.1061/(ASCE)ST.1943-541X.0003059.

Karacabeyli, E., and S. Gagnon. 2019. *Canadian CLT Handbook, 2019 Edition*. QC, Canada: Pointe-Claire. FPInnovations.

Khajehpour, M., Y. Pan, and T. Tannert. 2021. Seismic Analysis of Hybrid Steel Moment Frame CLT Shear Walls Structures. *Journal of Performance of Constructed Facilities* 35 (5): 04021059. doi:10.1061/(ASCE)CF.1943-5509.0001633.

K-net 2012 October. Strong-motion seismograph networks (k-net, kik-net). http://www.k-net.bosai.go.jp/

Koliou, M., A. Filiatrault, D. J. Kelly, and J. Lawson. 2016. Buildings with rigid walls and flexible roof diaphragms. I: Evaluation of current US seismic provisions. *Journal of Structural Engineering* 142 (3): 04015166. doi: 10.1061/(ASCE)ST.1943-541X.0001438.

Kovacs, M. A., and L. Wiebe. 2019. Controlled rocking CLT walls for buildings in regions of moderate seismicity: Design procedure and numerical collapse assessment. *Journal of Earthquake Engineering* 23 (5): 750–70. doi: 10.1080/13632469.2017.1326421.

Kramer, S. L. 1996. *Geotechnical earthquake engineering*. Prentice Hall: Pearson Education India.

Latour, M., and G. Rizzano. 2015. Cyclic behavior and modeling of a dissipative connector for cross-laminated timber panel buildings. *Journal of Earthquake Engineering* 19 (1): 137–71. doi: 10.1080/13632469.2014.948645.

Liu, J., and F. Lam. 2019. Experimental test of coupling effect on CLT hold-down connections. *Engineering Structures* 178: 586–602. doi: 10.1016/j.engstruct.2018.10.063.

Li, Z., X. Wang, and M. He. 2022. Experimental and analytical investigations into lateral performance of cross-laminated timber (CLT) shear walls with different construction methods. *Journal of Earthquake Engineering* 26 (7): 3724–3746.

Luo, J., M. He, Z. Li, J. Ou, and G. He. 2022. Seismic performance evaluation of glulam structures with either braced frames or knee-braced frames as the main lateral load resisting system. *Soil Dynamics and Earthquake Engineering* 154: 107134. doi: 10.1016/j.soildyn.2021.107134.

Mahdavifar, V., A. R. Barbosa, A. Sinha, L. Muszynski, R. Gupta, and S. E. Pryor. 2019. Hysteretic response of metal connections on hybrid cross-laminated timber panels. *Journal of Structural Engineering* 145 (1): 04018237. doi: 10.1061/(ASCE)ST.1943-541X.0002222.

Masroor, M., G. Doudak, and D. Casagrande. 2020. The effect of bi-axial behaviour of mechanical anchors on the lateral response of multi-panel CLT shearwalls. *Engineering Structures* 224: 111202. doi: 10.1016/j.engstruct.2020.111202.

Mazzoni, S., F. McKenna, M. H. Scott, and G. L. Fenves. 2006. *OpenSees command language manual, Pacific Earthquake Engineering Research (PEER) Center*, 137–58. Berkeley, CA: Pacific Earthquake Engineering Research Center.

Miller, S., J. E. Woods, J. Erochko, D. T. Lau, and C. F. Gilbert. 2021. Experimental and analytical fragility assessment of a combined heavy timber–steel-braced frame through hybrid simulation. *Earthquake Engineering & Structural Dynamics* 50 (2): 270–89. doi: 10.1002/eqe.3329.

NBCC. 2015. *National building code of Canada, Canadian commission on building and fire codes*. Ottawa, Ontario, Canada: National Research Council of Canada.

Pan, Y., C. E. Ventura, and T. Tannert. 2020. Damage index fragility assessment of low-rise light-frame wood buildings under long duration subduction earthquakes. *Structural Safety* 84: 101940. doi: 10.1016/j.strusafe.2020.101940.

PEER 2013 October. "Pacific Earthquake Engineering Research (PEER) NGA-West2 database." https://ngawest2.berkeley.edu/

Pei, S., J. W. van de Lindt, A. R. Barbosa, J. W. Berman, E. McDonnell, J. Daniel Dolan, H.-E. Blomgren, R. B. Zimmerman, D. Huang, and S. Wichman. 2019. Experimental seismic response of a resilient 2-story mass-timber building with post-tensioned rocking walls. *Journal of Structural Engineering* 145 (11): 04019120. doi: 10.1061/(ASCE)ST.1943-541X.0002382.

Popovski, M., I. Gavric, and J. Schneider 2014. "Performance of two-storey CLT house subjected to lateral loads." In *Proc., World Conference on Timber Engineering*. Quebec City, Canada.

Pozza, L., A. Saetta, M. Savoia, and D. Talledo. 2018. Angle bracket connections for CLT structures: Experimental characterization and numerical modelling. *Construction and Building Materials* 191: 95–113. doi: 10.1016/j.conbuildmat.2018.09.112.

Rinaldin, G., and M. Fragiacomo. 2016. Non-linear simulation of shaking-table tests on 3-and 7-storey X-Lam timber buildings. *Engineering Structures* 113: 133–48. doi: 10.1016/j.engstruct.2016.01.055.

Schneider, J., Y. Shen, S. Stiemer, and S. Tesfamariam. 2015. Assessment and comparison of experimental and numerical model studies of cross-laminated timber mechanical connections under cyclic loading. *Construction and Building Materials* 77: 197–212. doi: 10.1016/j.conbuildmat.2014.12.029.

Shahnewaz, M., C. Dickof, and T. Tannert. 2021. Seismic behavior of balloon frame CLT shear walls with different ledgers. *Journal of Structural Engineering* 147 (9): 04021137. doi: 10.1061/(ASCE)ST.1943-541X.0003106.

Shahnewaz, M., Y. Pan, M. Shahria Alam, and T. Tannert. 2020. Seismic fragility estimates for cross-laminated timber platform building. *Journal of Structural Engineering* 146 (12): 04020256. doi: 10.1061/(ASCE)ST.1943-541X.0002834.

Shahnewaz, M., M. Popovski, and T. Tannert. 2019. Resistance of cross-laminated timber shear walls for platform-type construction. *Journal of Structural Engineering* 145 (12): 04019149. doi: 10.1061/(ASCE)ST.1943-541X.0002413.

Sullivan, K., T. H. Miller, and R. Gupta. 2018. Behavior of cross-laminated timber diaphragm connections with self-tapping screws. *Engineering Structures* 168: 505–24. doi: 10.1016/j.engstruct.2018.04.094.

Sun, X., M. He, Z. Li, and Z. Shu. 2018. Performance evaluation of multi-storey cross-laminated timber structures under different earthquake hazard levels. *Journal of Wood Science* 64 (1): 23–39. doi: 10.1007/s10086-017-1667-7.

Tannert, T., M. Follesa, M. Fragiacomo, P. Gonzalez, H. Isoda, D. Moroder, H. Xiong, and J. van de Lindt. 2018. Seismic design of cross-laminated timber buildings. *Wood and Fiber Science* 50 (Special): 3–26. doi: 10.22382/wfs-2018-037.

Tesfamariam, S., K. Skandalos, K. Goda, M. A. Bezabeh, G. Bitsuamlak, and M. Popovski. 2021. Quantifying the ductility-related force modification factor for 10-story timber–RC hybrid building using FEMA P695 procedure and considering the 2015 NBC seismic hazard. *Journal of Structural Engineering* 147 (5): 04021052. doi: 10.1061/(ASCE)ST.1943-541X.0003007.

Vamvatsikos, D., and C. A. Cornell. 2002. Incremental dynamic analysis. *Earthquake Engineering & Structural Dynamics* 31 (3): 491–514. doi: 10.1002/eqe.141.

van de Lindt, J. W., M. O. Amini, D. Rammer, P. Line, S. Pei, and M. Popovski. 2020. Seismic performance factors for cross-laminated timber shear wall systems in the United States. *Journal of Structural Engineering* 146 (9): 04020172. doi: 10.1061/(ASCE)ST.1943-541X.0002718.

van de Lindt, J. W., J. Furley, M. O. Amini, S. Pei, G. Tamagnone, A. R. Barbosa, D. Rammer, P. Line, M. Fragiacomo, and M. Popovski. 2019. Experimental seismic behavior of a two-story CLT platform building. *Engineering Structures* 183: 408–22. doi: 10.1016/j.engstruct.2018.12.079.

Zhang, X., Y. Pan, and T. Tannert. 2021. The influence of connection stiffness on the dynamic properties and seismic performance of tall cross-laminated timber buildings. *Engineering Structures* 238: 112261. doi: 10.1016/j.engstruct.2021.112261.

Appendix: Hysteresis parameters of calibrated Pinching4 model

Parameters		HD1	HD2/3	SP1/2/3 (#1)	SP1/2/3 (#2)	SP7/8/9
Backbone	ePf1 (kN)	1.5	1.7	1.8	1.3	2.5
	ePf2 (kN)	3.3	3.0	4.0	2.0	5.0
	ePf3 (kN)	3.8	3.6	5.5	2.9	6.0
	ePf4 (kN)	3.0	3.3	5.0	2.0	4.0
	ePd1 (mm)	4.0	7.0	2.0	2.0	2.0
	ePd2 (mm)	13.0	15.0	9.0	8.0	16.0
	ePd3 (mm)	20.0	23.0	30.0	24.0	31.0
	ePd4 (mm)	25.0	27.0	40.0	34.0	40.0
	eNf1 (kN)	−1.5	−1.7	−1.8	−1.3	−2.5
	eNf2 (kN)	−3.3	−3.0	−4.0	−2.0	−5.0
	eNf3 (kN)	−3.8	−3.6	−5.5	−2.9	−6.0
	eNf4 (kN)	−3.0	−3.3	−5.0	−2.0	−4.0
	eNd1 (mm)	−4.0	−7.0	−2.0	−2.0	−2.0
	eNd2 (mm)	−13.0	−15.0	−9.0	−8.0	−16.0
	eNd3 (mm)	−20.0	−23.0	−30.0	−24.0	−31.0
	eNd4 (mm)	−25.0	−27.0	−40.0	−34.0	−40.0
Pinching	rDispP	0.70	0.65	0.60	0.70	0.75
	rForceP	0.15	0.15	0.25	0.28	0.25
	uForceP	0.02	−0.05	−0.02	0.02	−0.02
	rDispN	0.70	0.65	0.60	0.70	0.75
	rForceN	0.15	0.15	0.25	0.28	0.25
	uForceN	0.02	−0.05	−0.02	0.02	−0.02
Hysteresis	gK1	−0.5	−0.5	−2.0	−2.0	−2.0
	gK2	0	0	0	0	0
	gK3	0	0	0	0	0
	gK4	0	0	0	0	0
	gKLim	−1.0	−1.2	−1.0	−1.0	−1.0
	gD1	0.99	0.99	0.97	0.90	0.90
	gD2	0	0	0	0	0
	gD3	0	0	0	0	0
	gD4	0	0	0	0	0
	gDLim	0.03	0.03	0.10	0.10	0.10
	gF1	1	1	0	0	0
	gF2	0	0	0	0	0
	gF3	0	0	0	0	0
	gF4	0	0	0	0	0
	gFLmi	0.05	0.05	0.00	0.00	0.00
	gE	1	1	1	1	1
	damage	"energy"	"energy"	"energy"	"energy"	"energy"